Clouds and the Earth's Radiant Energy System (CERES)

Algorithm Theoretical Basis Document

Estimation of Longwave Surface Radiation Budget From CERES

(Subsystem 4.6.2)

CERES Science Team Surface Radiation Budget Working Group

Principal Investigators

A. K. Inamdar[1]
V. Ramanathan[1]

[1]Center for Clouds, Chemistry and Climate, Scripps Institution of Oceanography, University of California, San Diego, California

June 2, 1997

CERES Top Level Data Flow Diagram

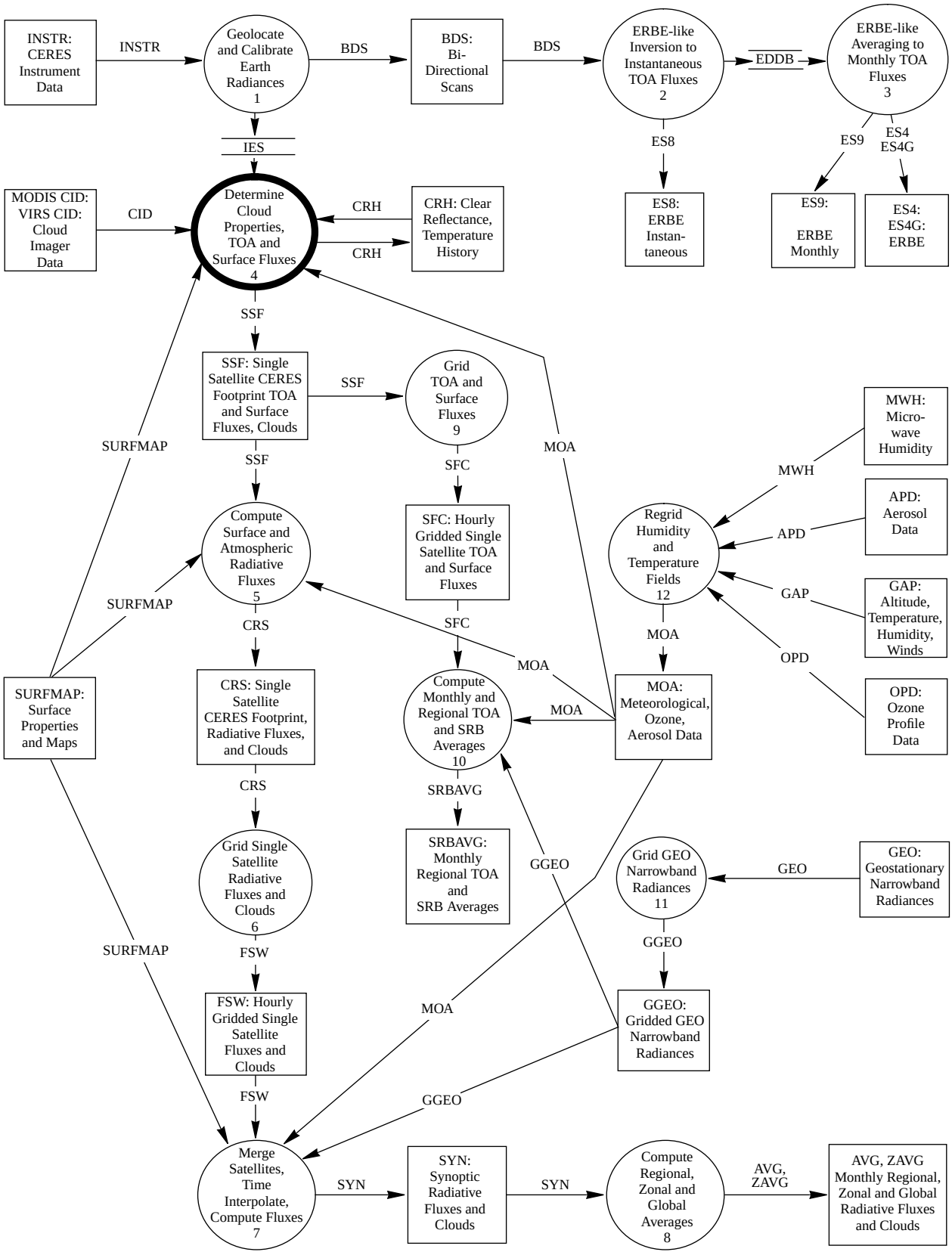

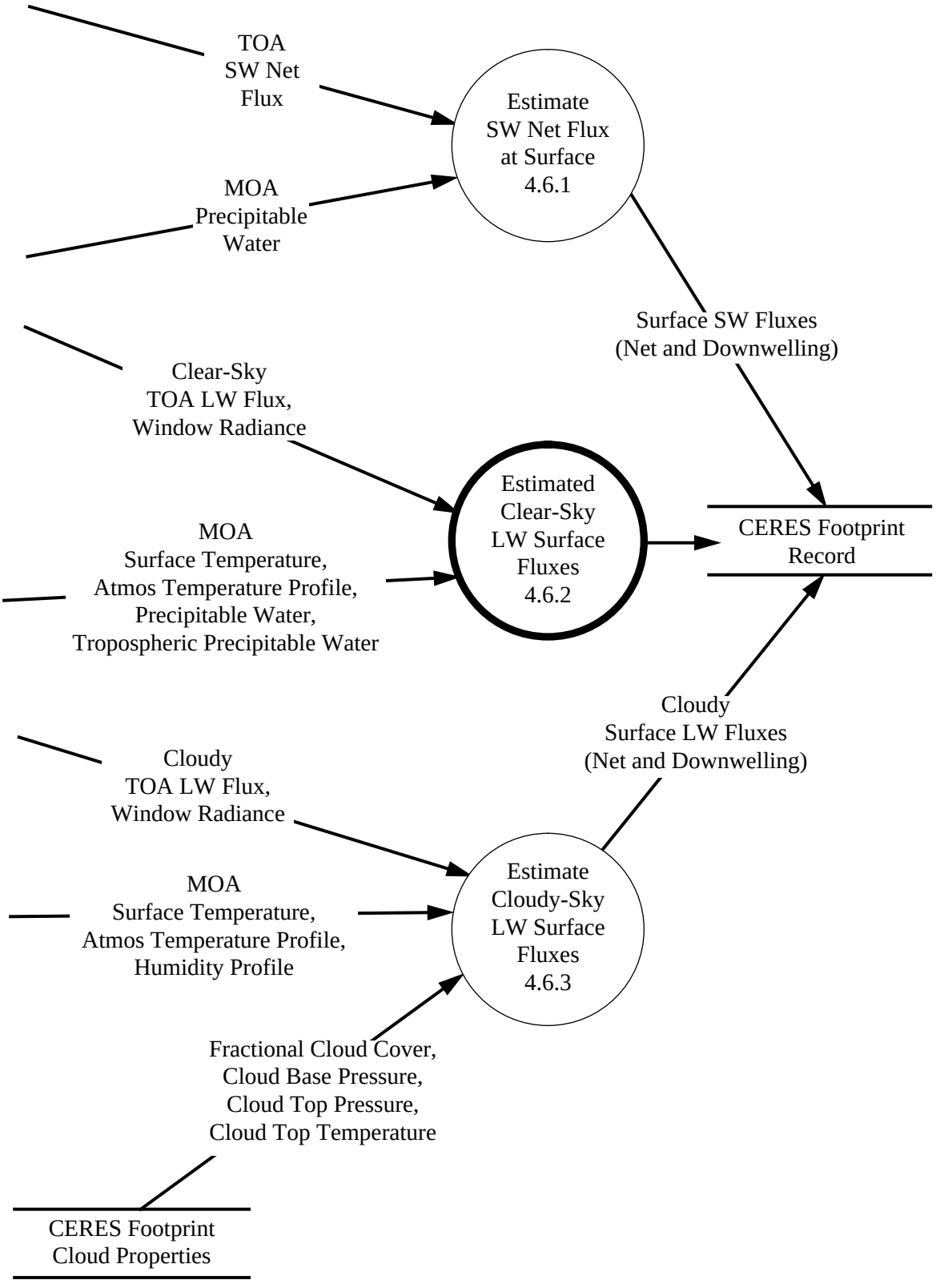
TOA
SW Net
Flux
MOA
Precipitable
Water
Estimate
SW Net Flux
at Surface
4.6.1
Surface SW Fluxes
(Net and Downwelling)
Clear-Sky
TOA LW Flux,
Window Radiance
Estimated
Clear-Sky
LW Surface
Fluxes
4.6.2
CERES Footprint
Record
MOA
Surface Temperature,
Atmos Temperature Profile,
Precipitable Water,
Tropospheric Precipitable Water
Cloudy
Surface LW Fluxes
(Net and Downwelling)
Cloudy
TOA LW Flux,
Window Radiance
Estimate
Cloudy-Sky
LW Surface
Fluxes
4.6.3
MOA
Surface Temperature,
Atmos Temperature Profile,
Humidity Profile
Fractional Cloud Cover,
Cloud Base Pressure,
Cloud Top Pressure,
Cloud Top Temperature
CERES Footprint
Cloud Properties

Abstract

This paper describes the status of the studies underway for the development of algorithms for surface longwave radiation budget using CERES instrumentation. The algorithm reported here uses a combination of TOA longwave fluxes measured by CERES and other correlated meteorological variables. CERES will estimate longwave fluxes in two spectral regions: broadband (4 to 500 μm) and window (8 to 12 μm).

A radiative transfer model was used to simulate the TOA and surface longwave fluxes and choose the algorithm. The input to the model is sondes launched from ships. The complete algorithm relates the longwave down flux at the surface in terms of four parameters: TOA broadband and window flux, the total column water vapor, the surface temperature, and the near-surface atmospheric temperature. The rms errors in the predicted surface fluxes (pole to pole) range between 3 and 4.5 W-m^{-2}. The model and algorithm have been validated with field data collected during the Central Equatorial Pacific Experiment (CEPEX) and ARM Probe sites.

4.6.2. Estimation of Longwave Surface Radiation Budget From CERES

Symbols

F_0^+	surface black body emission $\approx \sigma T_s^4$
F_0^-	downward longwave flux at the surface, W-m^{-2}
$^*F_\infty^+$	longwave flux at TOA, W-m^{-2}
f_0^-	normalized F_0^- where $f_0^- = F_0^-/F_0^+$
f_∞^+	normalized F_∞^+ where $f_\infty^+ = F_\infty^+/F_0^+$
G_a	clear-sky greenhouse effect of the atmosphere where $G_a = F_0^+ - F_\infty^+$
g_a	normalized G_a where $g_a = G_a/F_0^+ = 1 - f_\infty^+$
I_0^-	downwelling radiance in the 500 to 2000 cm^{-1} range, W-m^{-2}-sterad^{-1}
T_a	atmospheric temperature, subscript indicates the pressure level
T_s	surface temperature, K
w_{tot}	total column precipitable water, g-cm^{-2}
τ_{vis}	aerosol optical depth in the visible (0.55 μm)

4.6.2.1. Introduction

The methods used for deriving the surface longwave radiation budget can be classified as physical, empirical, or statistical. The physical methods are based on the application of the full radiative transfer theory (Frouin et al. 1988; Darnell et al. 1983; Wu and Cheng 1989) using the profiles of temperature, humidity, and molecular species in the atmosphere. These profiles are retrieved from satellite (NOAA

[*] The second subscripts "*win*" and "*nw*" for any flux parameter denote the corresponding quantities integrated over the window (8–12 μm) and nonwindow spectral intervals, respectively.

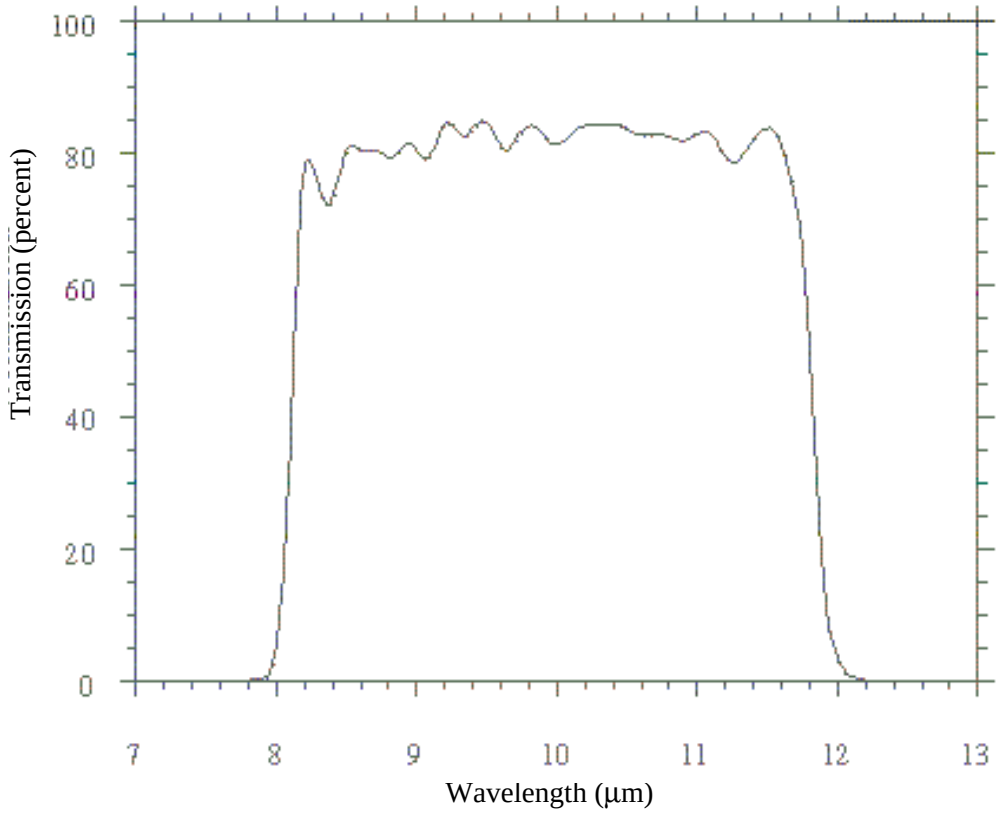

Figure 1. Combined longwave filter transmission (average of both front and rear filters).

TOVS) radiance data. Errors in the retrieved parameters limit the accuracy of the surface fluxes. Numerous simple empirical relationships (Brutsaert 1975; Idso 1981; Schmetz et al. 1986; Tuzet, 1990) have employed an effective sky-emittance temperature to predict the downward flux. These relationships depend on the temperature and partial pressure of water vapor (Idso 1981) near the surface, but a drawback is that they apply to only a selected range of surface temperatures. Statistical methods, on the other hand, use a combination of top-of-the-atmosphere spectral radiances measured by AVHRR/HIRS-2-type instruments and obtain surface fluxes through regression techniques (Schmetz 1986; Gupta 1989).

Our method is a variant of the statistical technique and is developed for the CERES instrument. Because our method is geared toward CERES instruments, a brief description of CERES longwave measurement will be given first.

4.6.2.1.1. CERES longwave measurements. CERES uses a pair of broadband scanning radiometers. The radiometers have a total band (shortwave + longwave) and shortwave and longwave window channels. The broadband (4 to 500 μm) longwave flux is obtained from a combination of all of the three channels. The spectral response characteristic of the longwave window channel is shown in figure 1. For reference, the atmospheric transmittance is shown in figure 2. The sensor has a nominal optical spectral bandpass from 8 to 12 microns that is formed by a filter of multilayer dielectric interference stacks. A combination of two filters is used.

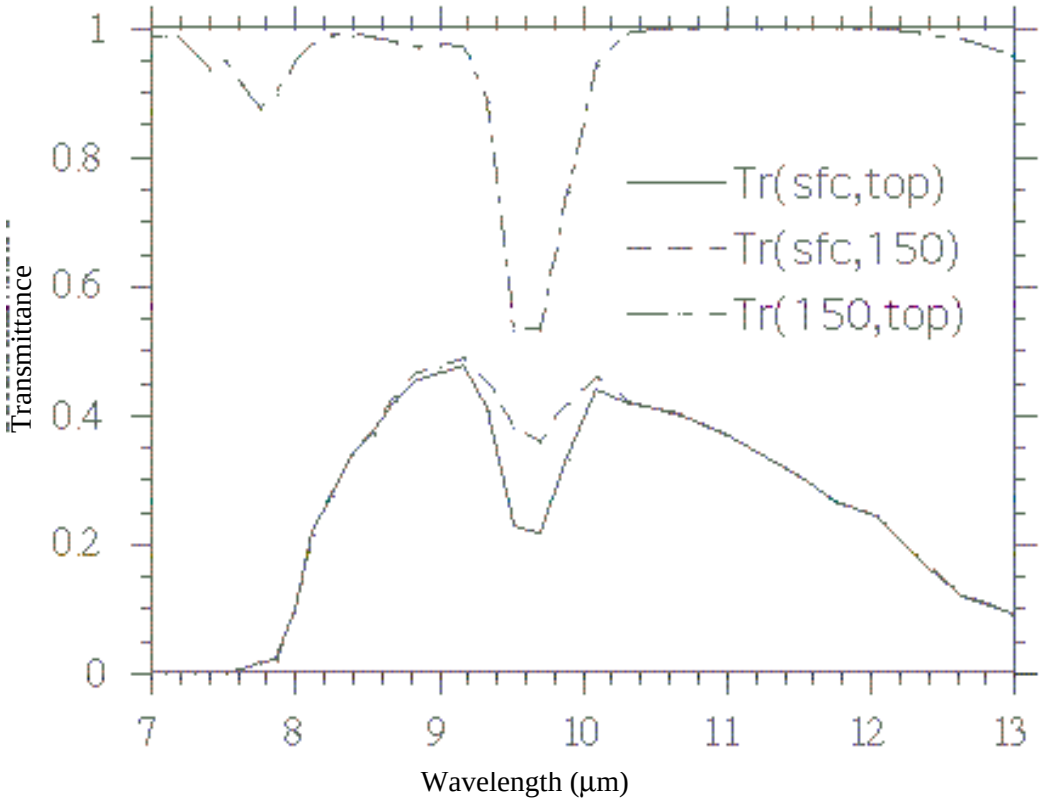

Figure 2. Atmospheric transmittances from 7 to 13 μm (sfc, top, and 150 refer to the surface, top of atmosphere, and 150-mb levels, respectively).

4.6.2.2. Clear-Sky Downward Surface Flux

The basis of our algorithm is model calculation of longwave fluxes (both broadband and window) at the TOA and the surface. These calculations use soundings deployed from ships.

4.6.2.2.1. Model simulation and data. The greenhouse effect and the downward flux density at the surface can be expressed by using the integral form of the solution to the equation of radiative transfer as

$$G_a = \int_{z_{top}}^{0} A(z_{top}, z') \frac{dB(z')}{dz'} dz' \tag{1}$$

$$F_a^- = B(z_{top}) A(z_{top}, 0) - \int_{0}^{z_{top}} A(0, z') \frac{dB(z')}{dz'} dz' \tag{2}$$

where z is the altitude, $B(z')$ is the Planck blackbody function, $A(z, z')$ is the atmospheric absorptance between the levels specified in the arguments, and z_{top} is the altitude at the top of atmosphere. The absorptance A, and hence F_a^-, is the result of absorption and emission by water vapor, CO_2 ozone, CH_4, N_2O, and trace gases and scattering by aerosols and water droplets in the entire atmospheric column. It depends on the vertical distribution of temperature, as well as molecular species, including water vapor, in the atmosphere. The transmittances have been computed using the 20 cm^{-1} LOWTRAN 7 (Kneizys

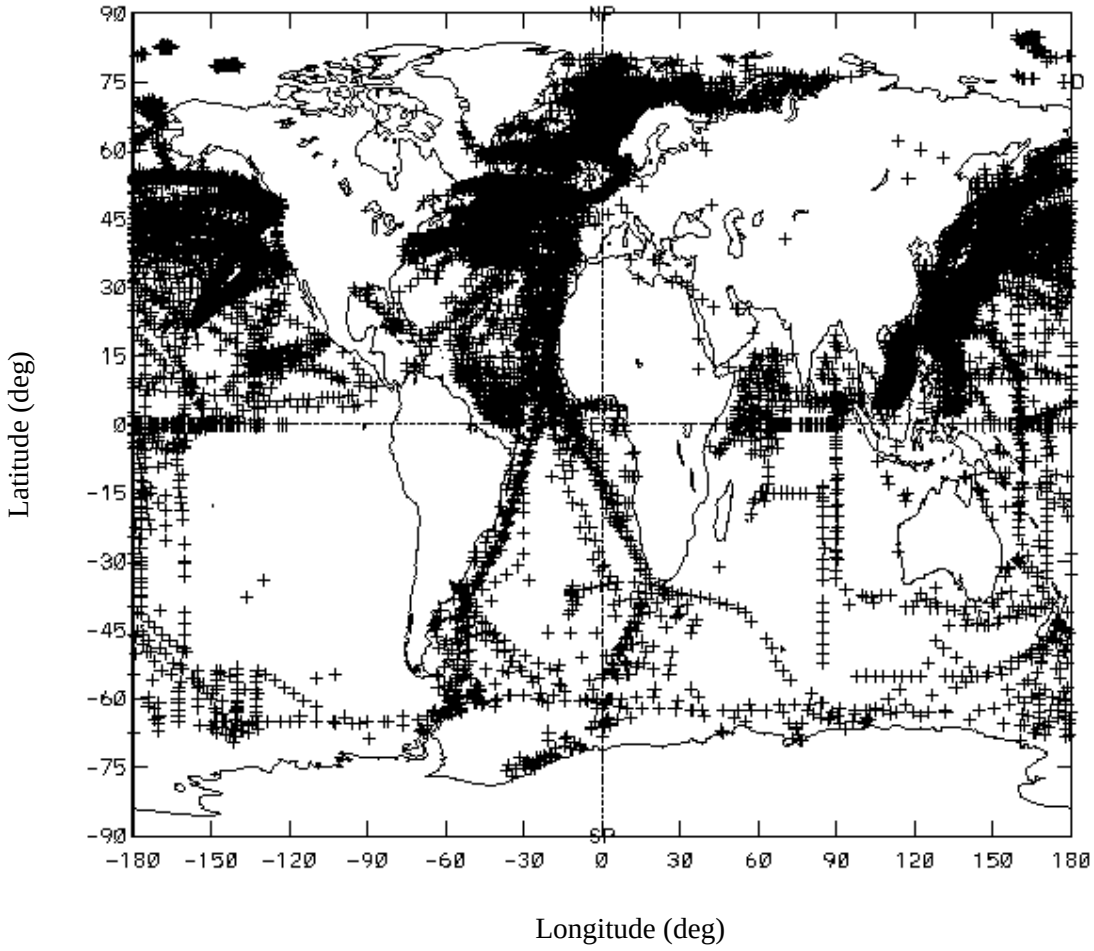

Figure 3. Ship data locations (1985 to 1989) over the global oceans used in this study.

et al. 1988) transmittance code. However, the continuum model used in LOWTRAN 7 has been updated including a revised version (May 1994) of the Clough-Kneizys-Davies (CKD) model (Clough et al. 1989). Revisions effected in both the self- and foreign-continuum coefficients (Clough and Brown 1995) to the data of Burch in the 1300 cm^{-1} region have been validated against HIS spectra downlooking from 20 km and uplooking from the surface. Equations (1) and (2) are evaluated using a quadrature scheme and a high vertical resolution equivalent to a vertical layer spacing ranging from a minimum of 1 mb to a maximum of 1/4 km. Agreement of the boundary fluxes using the ICRCCM standard atmospheres (Ellingson 1991) as input is within 2 to 3 $W\text{-}m^{-2}$.

The input data used for this study consist of the ship rawinsondes for the years 1985 to 1989—to coincide with the Earth Radiation Budget Experiment (ERBE) observations for the same period—obtained from the NCAR NMC upper air data base. The locations of ship data over the entire globe used in this study is shown in figure 3. There is a fair distribution of data points to exclude any sampling-related problems in the analysis. The poor quality of humidity values above 5 to 6 km reported from soundings is well known (Elliot and Gaffen 1991). An error analysis, using the standard deviation of errors as reported by field tests of radiosonde instruments (Inamdar and Ramanathan 1994),

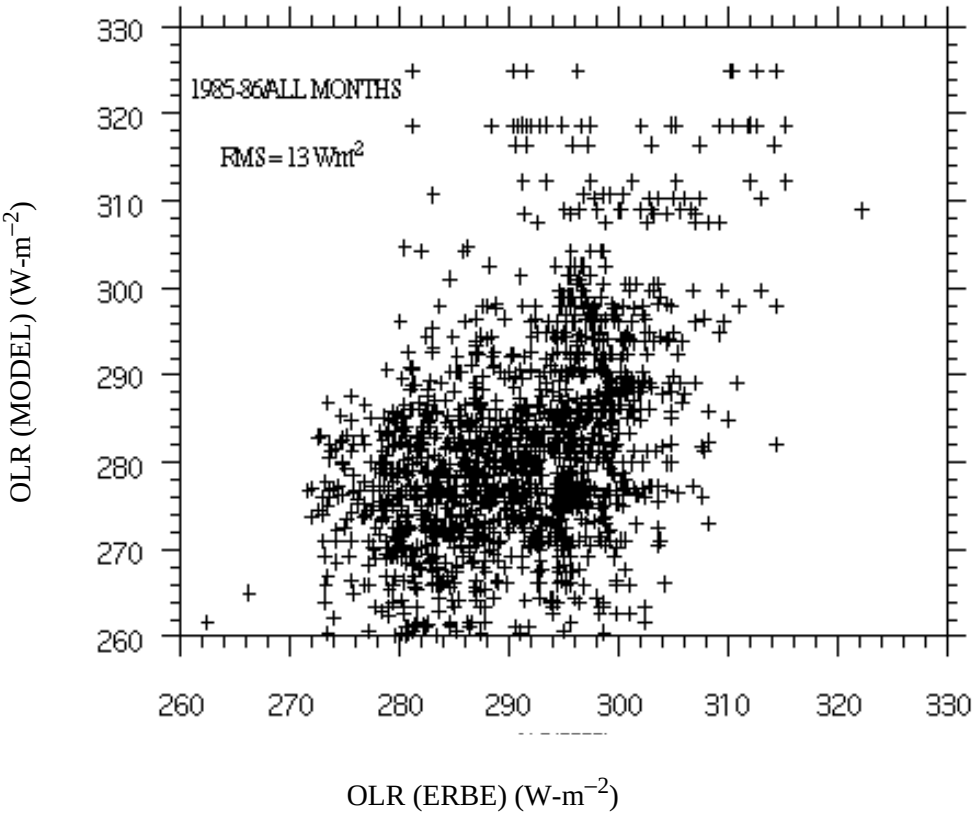

Figure 4. Comparison of model-derived longwave fluxes at TOA for 1985 ship data with collocated ERBE measurements.

showed the error to be distributed between 6% near the surface to nearly 13% at about 200 mb. Humidity data above 200 mb have not been used. To establish the fidelity of sonde data, an independent validation has been performed by employing the Earth Radiation Budget Experiment (ERBE) data. We use the daily clear-sky ERBE OLR data for 1985 extracted from the hour-box record in the same time window (within 24 hr) and location as the ship data. The comparison shown in figure 4 in the form of a scatter plot between ERBE and model TOA fluxes is within the uncertainty limits of the former.

4.6.2.2.2. Parameterization. We begin the process of parameterization by first performing the radiative transfer simulations through equations (1) and (2) and employing ship sondes as input, to derive the TOA and surface longwave fluxes. We first fit the window and nonwindow components of downward flux in terms of the respective components of greenhouse effect as

$$f^{-}_{0,\,win} = a_0 g_{a,\,win} + a_1 \tag{3}$$

$$f^{-}_{0,\,nw} = b_0 g_{a,\,nw} + b_1 \tag{4}$$

and next focus on seeking an optimum combination of parameters, P_i (see table 1), that best fit the deviations of window and nonwindow fluxes as predicted from (3) and (4) from the actual fluxes:

Table 1. Parameterization Equations

Model	Equation	Comments
Tropics (30°S to 30°N)	$f^-_{0,win} = 3.2504 g_{a,win} + [0.1377 w_{tot} + 3.46305 \ln(f^+_{\infty,win}/f^+_{0,win}) + 0.13866(T_s/300) + 1.12813(T_{950}/300)] f^+_{\infty,win} - 0.24155$	Window rms error 3.3 W-m^{-2}
	$f^-_{0,nw} = 0.25878 g_{a,nw} + [0.07363 \ln(w_{tot}) - 1.09875(T_s/300) + 1.442(T_{950}/300)] f^+_{\infty,nw} + 0.45445$	Nonwindow rms error 1.7 W-m^{-2}
	$f^-_0 = f^-_{0,win} + f^-_{0,nw}$	Total rms error 4.4 W-m^{-2}
Extra Tropics (30° to Pole)	$f^-_{0,win} = 1.6525 g_{a,win} + [0.15385 w_{tot} + 2.0074 \ln(f^+_{\infty,win}/f^+_{0,win}) - 0.29873(T_s/300) + 0.52062(T_{950}/300)] f^+_{\infty,win} - 0.01875$	Window rms error 1.7 W-m^{-2}
	$f^-_{0,nw} = 0.12284 g_{a,nw} + [0.07748 \ln(w_{tot}) - 1.52282(T_s/300) + 1.81629(T_{950}/300)] f^+_{\infty,nw} + 0.52066$	Nonwindow rms error 2.0 W-m^{-2}
	$f^-_0 = f^-_{0,win} + f^-_{0,nw}$	Total rms error 3.2 W-m^{-2}

$$f^-_{0,win} - a_0 g_{a,win} = c_0 + f^+_{\infty,win} \sum_i c_i P_i \tag{5}$$

$$f^-_{0,nw} - b_0 g_{a,nw} = d_0 + f^+_{\infty,nw} \sum_i d_i P_i \tag{6}$$

where the c_i and d_i are constants to be determined through regression analyses. The combination of parameters, P_i, have been chosen after a careful investigation of the physics of the problem and extensive sensitivity studies (described briefly below) to identify the parameters contributing most to the variability of the downward flux.

The physics of radiative transfer in the window and nonwindow spectral regions forms the basis of our algorithm. The close correlation between the atmospheric greenhouse effect (G_a) and the downward emissions (Inamdar and Ramanathan 1994) leads us to choose the window and nonwindow components of G_a as the key radiometric quantities in the parameterization. Note that a two-step procedure is followed [the pair of equations (3), (5) and (4), (6)] in predicting each component of the downward flux. Although a single step regression could have yielded a similar or even better accuracy, this two-step procedure forces the coefficients of the window and nonwindow components of greenhouse effect to bear the bulk of the burden in variability associated with atmospheric temperature and water vapor. This procedure partially alleviates problems related to the contamination of clear-sky TOA fluxes with thin cirrus. For instance, a direct regression would assign a higher weight to the coefficients of temperature terms, and application of the algorithm could be misconstrued to interpret any lower values of OLR as emanating from a colder atmosphere.

In the opaque nonwindow spectral regions, the atmospheric absorption attains saturation close to the surface, and hence it is the near-surface emissions that determine the down flux. In fact more than 95% of the total downward flux originates in the first few kilometers. Further, following the work of Cess and Tiwari (1972), the column absorption resulting from vibration-rotation bands in the nonwindow can be best described in the logarithmic limit. The column absorption in the window is highly sensitive to the vertical distribution of moisture and can be expressed as a combination of a linear limit and a temperature-dependence factor. Because transmittance in the window is very nearly exponential,

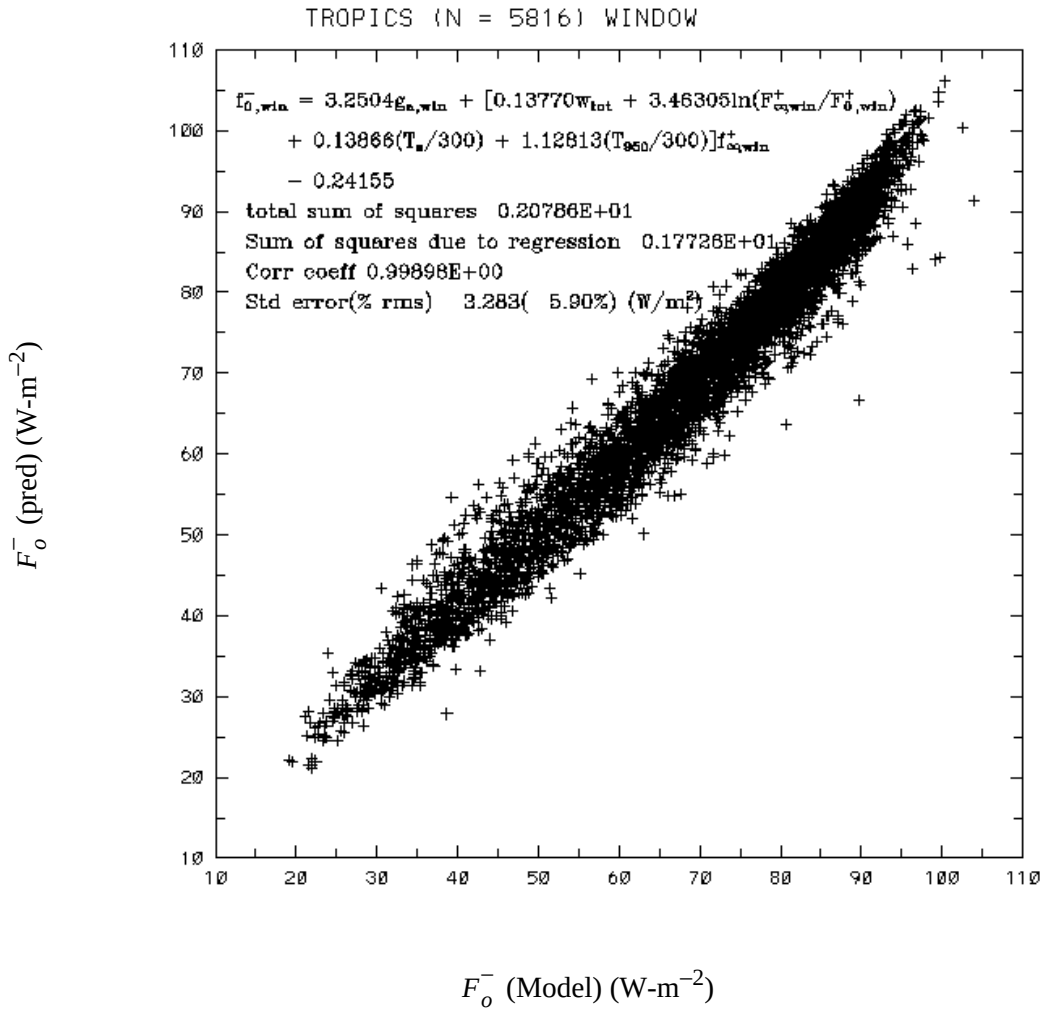

Figure 5. Comparison of clear-sky downward longwave fluxes predicted from the parameterized model 1 (recommended) with those from the detailed radiative transfer calculations over the tropics.

the ratio of window component of top-of-atmosphere to surface emissions yields an approximate measure of the optical depth. The surface temperature and the air temperature in the vicinity of the surface (950 mb in this case), were chosen to account for the flux variances that were not explained by the flux and water vapor terms.

In summary, we propose our standard model in terms of the window and nonwindow components of g_a, $\ln(w_{tot})$, w_{tot}, $\ln(F^+_{\infty,\,win}/F^+_{0,\,win})$, T_s, and T_a. All of the radiative flux parameters have been normalized (Raval and Ramanathan 1989) with the surface blackbody emission to eliminate the surface temperature dependence. Regression analysis of the radiative transfer-simulated fluxes has been performed separately for the tropics (30°S to 30°N) and extratropics (30° to poles) to accommodate the different physics and thus achieve better accuracy. Table 1 and figures 5 to 10 present a summary of the recommended models. Inputs for the model are, in addition to the CERES broadband and window channel information, data on temperature and the total column water vapor, w_{tot} (g-cm^{-2}) derived either through instruments such as the Special Sensor Microwave Imager (SSMI) measurements over the oceans, microwave sensors aboard the Defense Meteorological Space Program (DMSP) satellite, or from detailed water

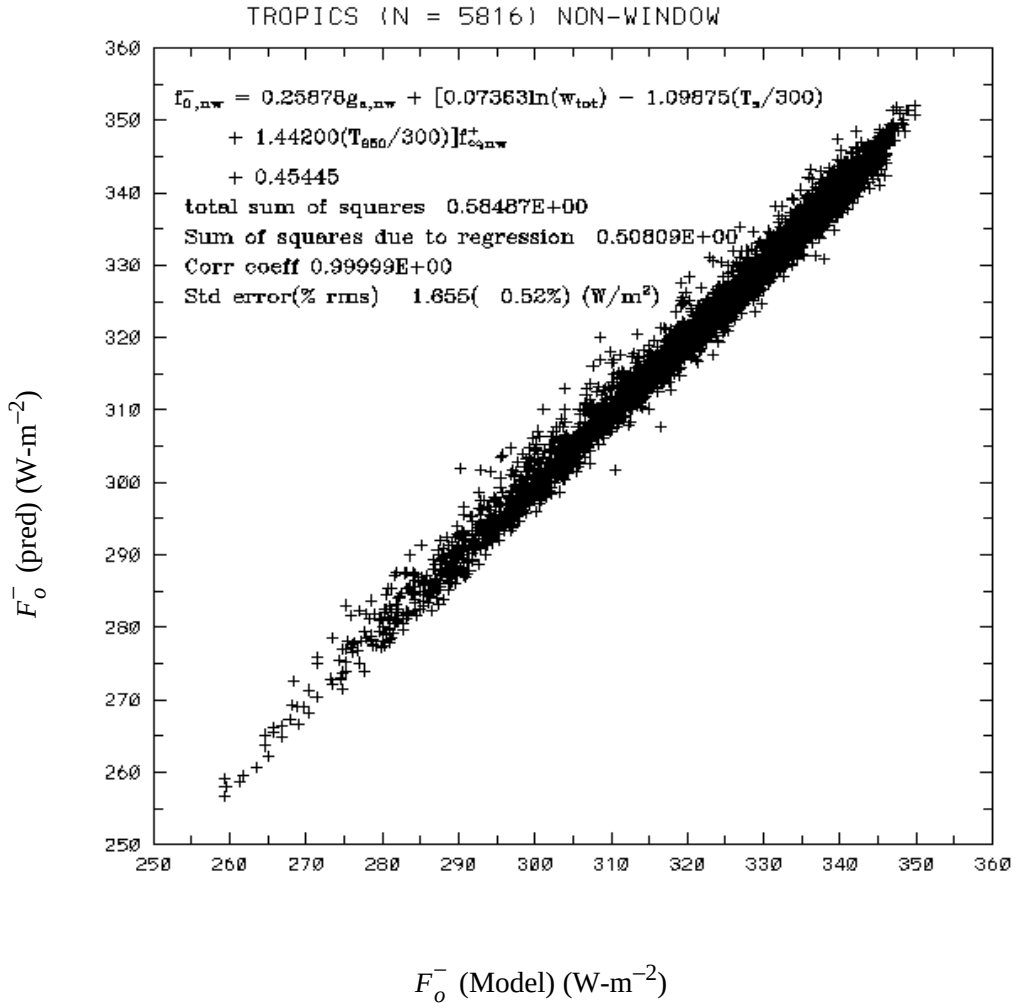

Figure 6. Same as in figure 5, but for extratropics.

vapor profiles derived from the TOVS data products. It is to be noted from figures 5 to 10 that the coefficients of $g_{a,win}$ and the window flux ratio term dominate in the tropics and explain the bulk of the variability. The combination of residual parameters of water vapor, temperature, and window flux ratio appearing in brackets are multiplied by the respective components of outgoing longwave flux to explain the nonlinear variability in g_a at higher temperatures. The standard error between the radiative fluxes derived from the full radiative transfer model [F^-_0 (Model) in fig. 5] and that predicted by the parameterization [F^-_0 (pred)], is about 4.4 W-m^{-2} for the tropics and 3.2 W-m^{-2} for the extratropics. The terms "total sum of squares," $\Sigma[f^-_0(\text{model}) - \bar{f}^-_0]^2$; "sum of squares due to regression," $\Sigma[f^-_0(\text{pred}) - \bar{f}^-_0]^2$, where $\bar{f}^-_0$ is a mean value of $\bar{f}^-_0$ (model); and correlation coefficient shown in figures 5 to 10 represent statistical measures of the goodness of fit. A comparison of the former two terms reveals how closely the chosen parameters explain the total variance of the predicted quantity. The correlation between the model and predicted fluxes is very high (0.9998) and the regression line is extremely close to the 45° line, indicating the absence of any bias in the parameterized flux estimates.

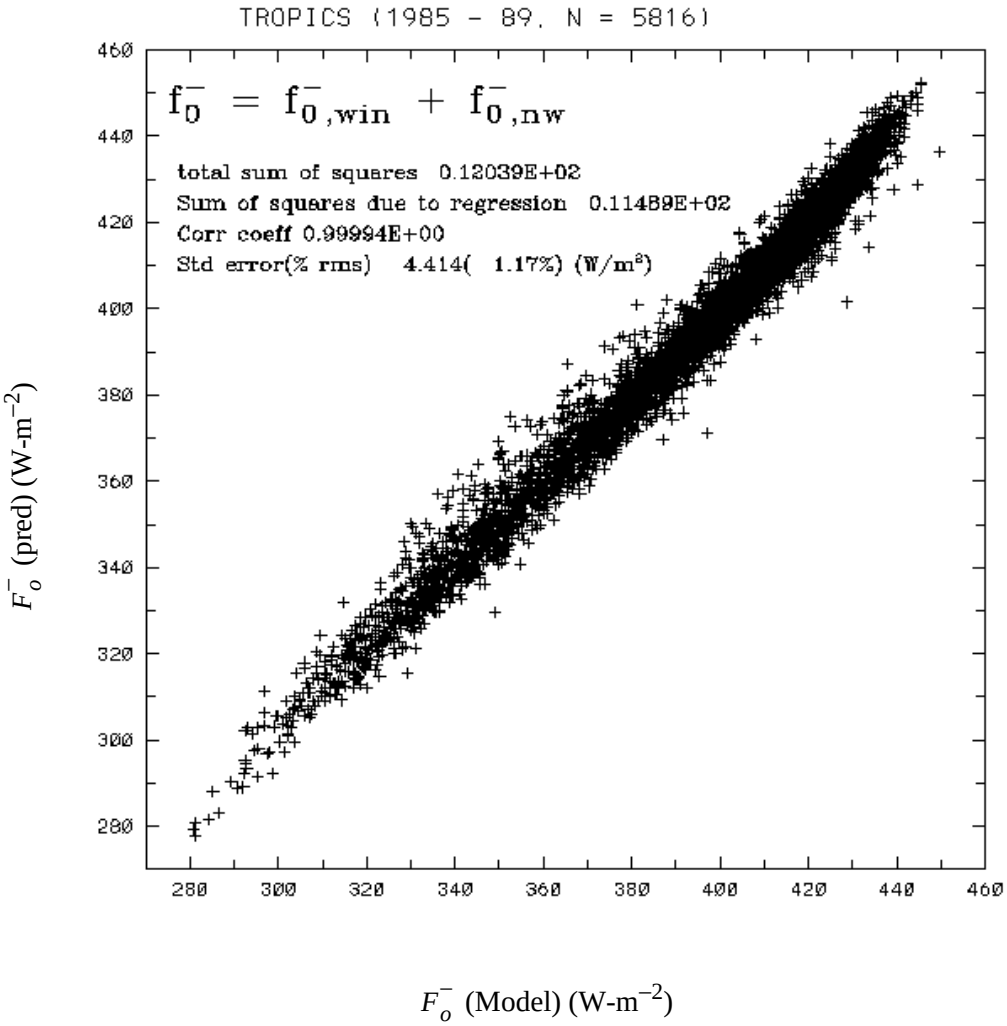

Figure 7. Same as in figure 5, but for model 2 (table 1).

4.6.2.3. Validation

The data sources used in the validation exercise come from the Central Equatorial Pacific Experiment (CEPEX) conducted in March/April 1993, which was a multiplatform endeavor, and also measurements made during the Intensive Observation Period (November 1992 to February 1993) at the Kavieng island site as part of the TOGA/ISS program.

The research vessel Vickers, with a cruise track along the equator starting from Honiara (160°E, 10°S) to the Christmas islands (160°W, 5°N), made state-of-the-art measurements of temperature, humidity, and ozone mixing ratios between March 8 and 21, 1993. The ship also had aboard a Fourier Transform Infrared Spectroradiometer (FTIR) measuring the narrow field of view (Lubin 1994) incoming longwave radiance in the 5- to 20-μm region, and in addition an Eppley Pyrgeometer to measure the broadband longwave fluxes. The FTIR radiances are converted to broadband fluxes using the following procedure: Vickers soundings are used as input and equation (2) is used to simulate both the broadband longwave fluxes and the 5- to 20-μm radiances under clear skies. A plot of these (fig. 11) indicated an excellent quadratic fit with a correlation coefficient of 0.999. The broad band fluxes derived from this relation are referred to as “FTIR fluxes” and form the basis of our comparison. The comparison is

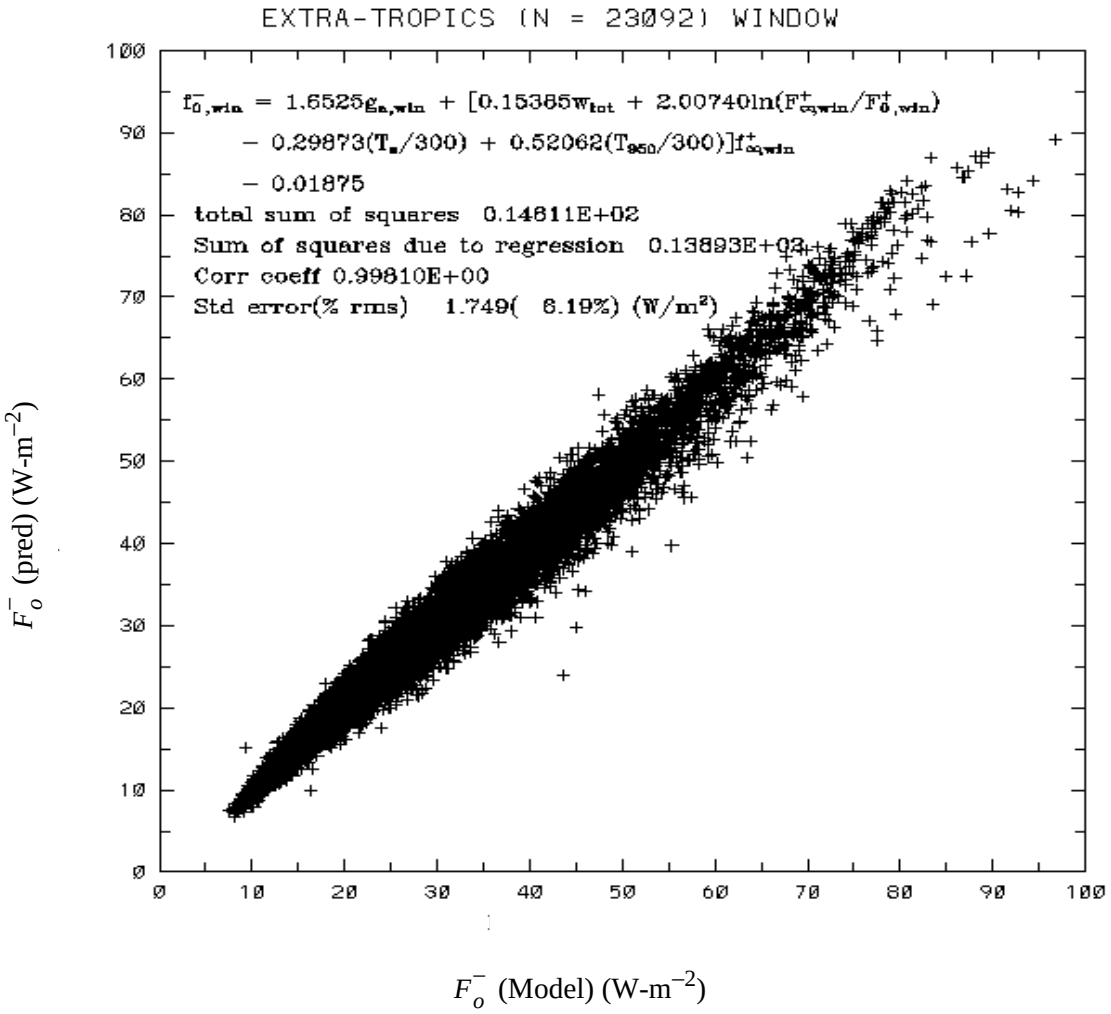

Figure 8. Same as in figure 7, but for the extratropics.

restricted to the days identified as “clear skies” by visual observations of overhead sky conditions aboard the ship. Top-of-atmosphere fluxes are derived from the infrared brightness temperatures measured by the Japanese Geostationery Meteorological Satellite (GMS) collocated with the Vickers ship. The infrared brightness temperatures have been converted after correcting for the limb-darkening effects to yield both the window (8- to 12-mm) channel and broadband flux using regression relations between the variables derived from model simulations. These GMS-derived window and broadband TOA fluxes and temperature and total precipitable water obtained from the Vickers sondes form the input to the algorithm. One must remember here the inherent limitations of the TOA fluxes as, in reality, both the flux components are derived from only one independent measure (namely the infrared brightness temperature). There is also evidence of contamination by thin cirrus clouds (see lower panel) as indicated by wide differences with the model simulations. Despite these shortcomings, the agreement of the algorithm-predicted fluxes is pretty good not only with the model, but also the FTIR and Pyrgeometer measurements (top panel). Although there is a systematic difference with the FTIR fluxes, the disparities between the FTIR and the collocated Pyrgeometer suggest a calibration-related uncertainty in FTIR of nearly 5 to 8 W-m^{-2}.

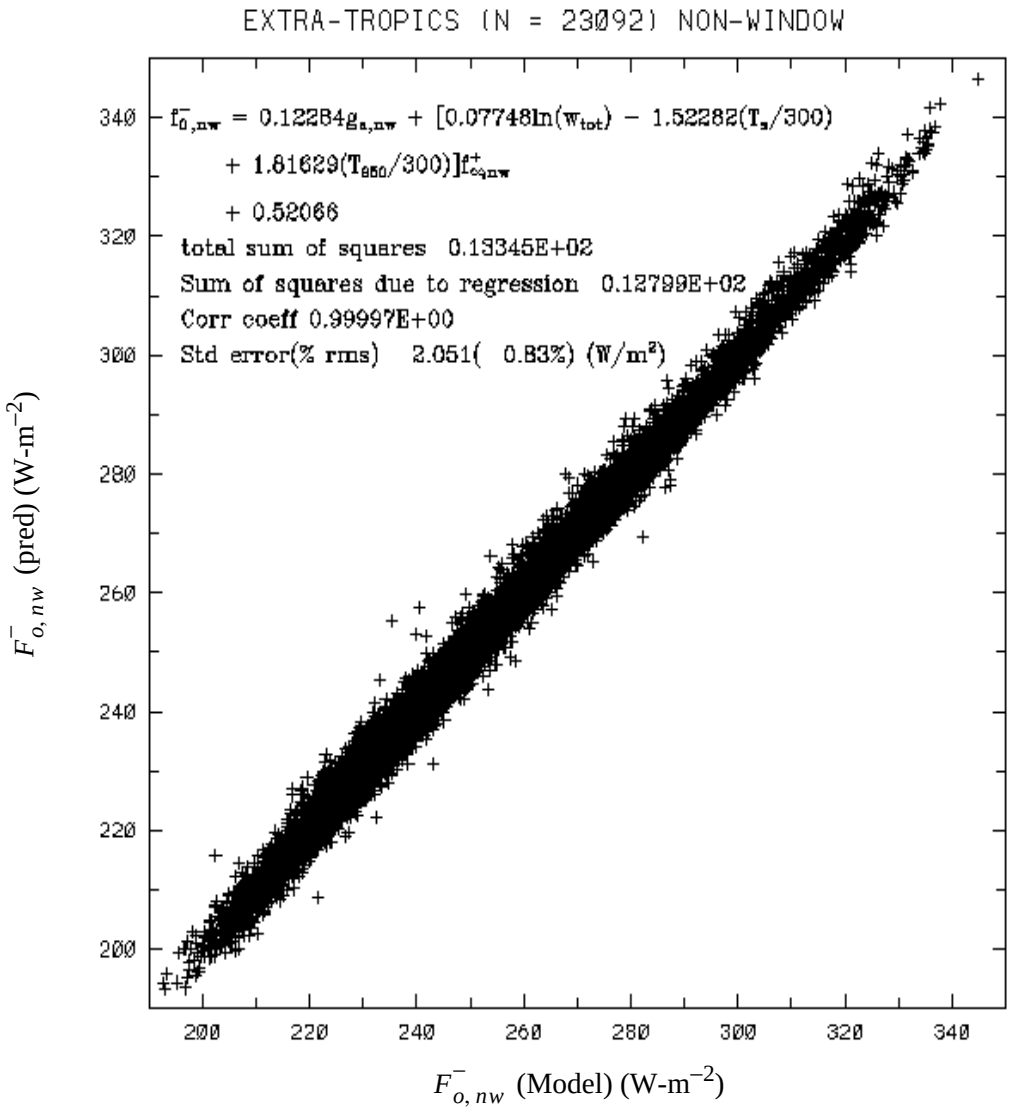

Figure 9. Same as in figure 6, but for the extratropics.

The next data set used in our validation exercise is the broadband flux and sonde measurements at Kavieng island (151°E, 2.5°S) in the western pacific. Unlike the CEPEX, the algorithm predictions are not constrained by the TOA flux measurements, and here we recourse to the model-derived outgoing longwave fluxes instead. Comparisons are restricted to the daytime only, where clear-sky scenes are identified through concurrent observations of shortwave radiation. The scheme followed for scene identification is based on choosing a threshold value (Chuck Long, personal communication) for the ratio of diffuse to global incident (direct + diffuse) solar flux at the surface. This threshold value is a function of the solar zenith angle and obtains from an empirical relationship derived from a statistical analyses of 5 minute bin-averaged data of shortwave radiation fluxes. An interesting observation from figures 12 and 13 is the opposite signs of the slight bias observed in the algorithm estimates of flux, reflecting the uncertainties related to the instrument calibration and also the quality or bias of sonde measurements in the two separate field experiments. The algorithm is seen to perform reasonably well (fig. 13) with the mean difference being 3 W-m^{-2} and an rms difference of about 10 W-m^{-2}.

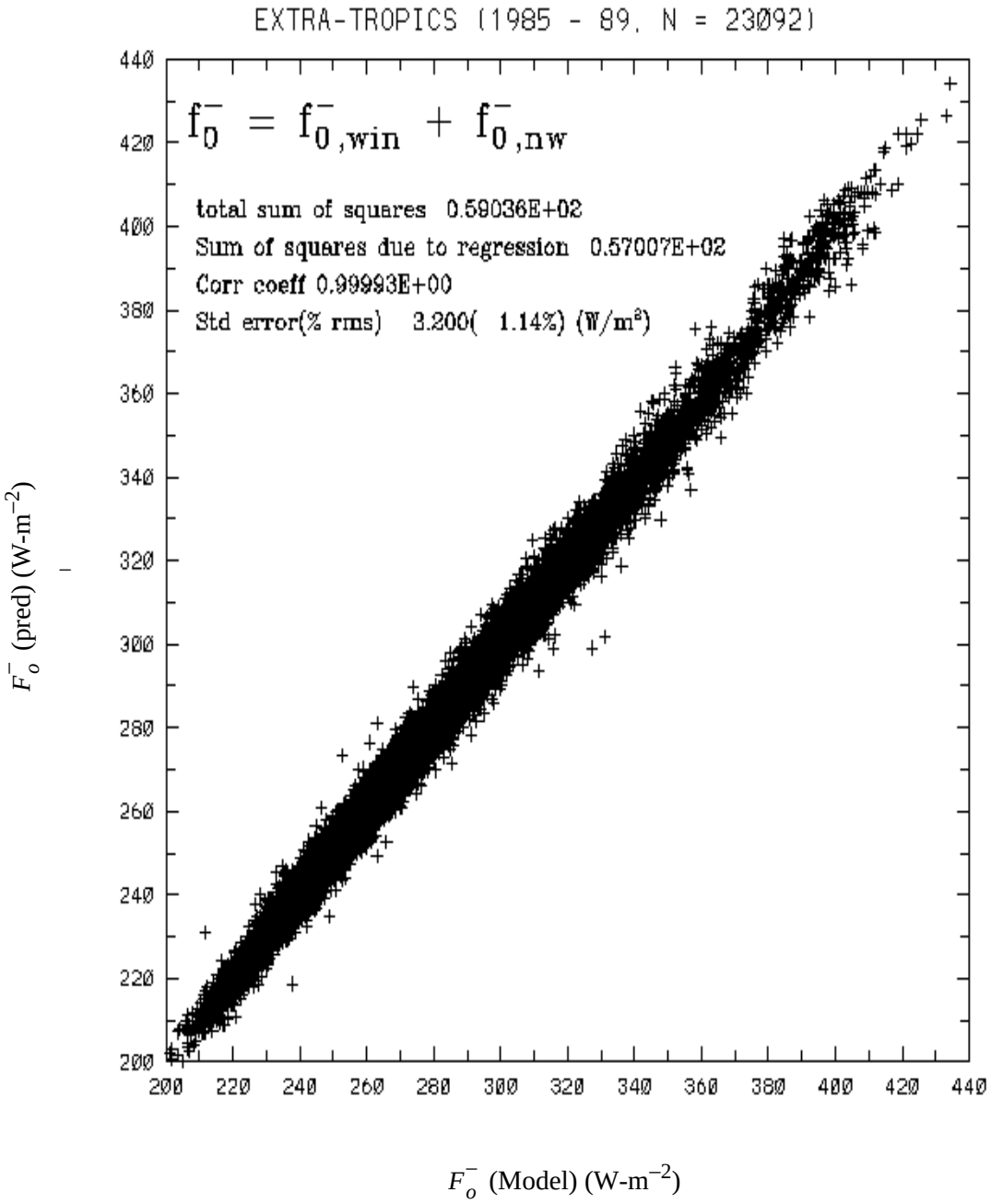

Figure 10. Same as in figure 7, but for the extratropics.

4.6.2.4. Conclusion

This work describes the methods to derive the clear-sky downward longwave flux at the surface from CERES broadband and window channel TOA flux measurements, atmospheric temperature data at 950 mb level, and total column water vapor information. The detailed radiative transfer simulations have been performed using 5 years (1985 to 1989) of ship sondes as input. The simulated outgoing longwave fluxes agree with the collocated ERBE data with an rms error of about 13 W-m^{-2}, which is

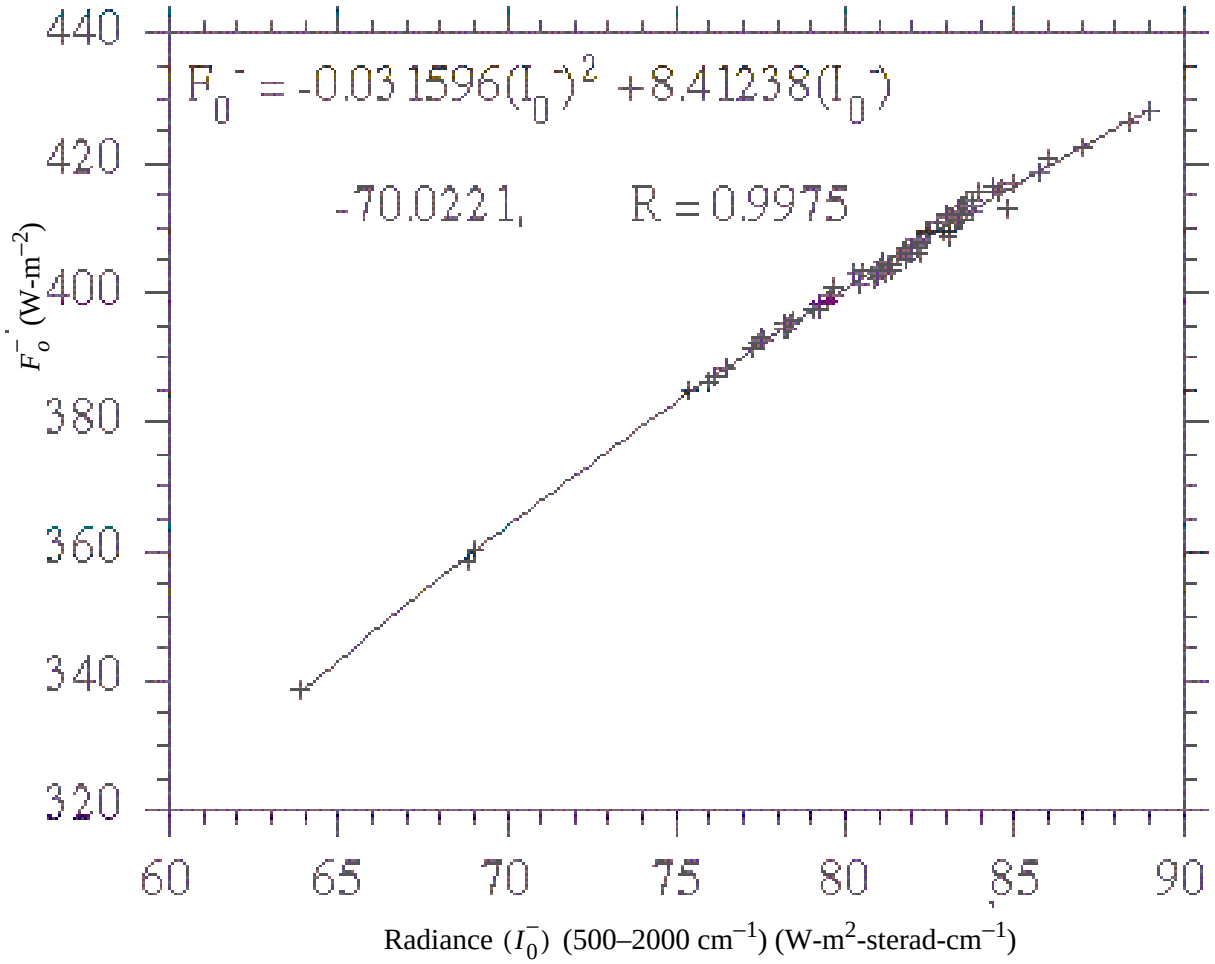

Figure 11. Model-simulated broadband fluxes and radiances for FTIR spectral range of 5 to 20 μm for Vickers sondes.

within the uncertainties of ERBE fluxes. The parameterizations exploit the physics of radiative transfer in the window and nonwindow spectral regions. Because of the close affinity of the downward flux with the greenhouse effect, the downward emissions in the window and nonwindow are first constrained in terms of their respective components of greenhouse effect, and in the second step the deviation of the predicted flux is explained in terms of the other residual variables. Column absorption in the nonwindow varies as the logarithm of the absorber amount, whereas the window component varies in the linear limit and is highly sensitive to the vertical distribution of moisture. The effect of continuum, which dominates in the tropics, is proportional linearly to the column water vapor and the logarithm of TOA and surface flux ratio in the window, the latter constituting a measure of the optical depth. The tropics (30° S to 30° N) and extratropics (30° to poles) have been treated separately because of the differences in the physics and to achieve the best accuracy. The rms accuracies obtained range between 3 and 4.5 W-m^{-2}, and the correlation coefficient between the radiative transfer-simulated fluxes and that predicted by the parameterization has been found to be very high (0.999).

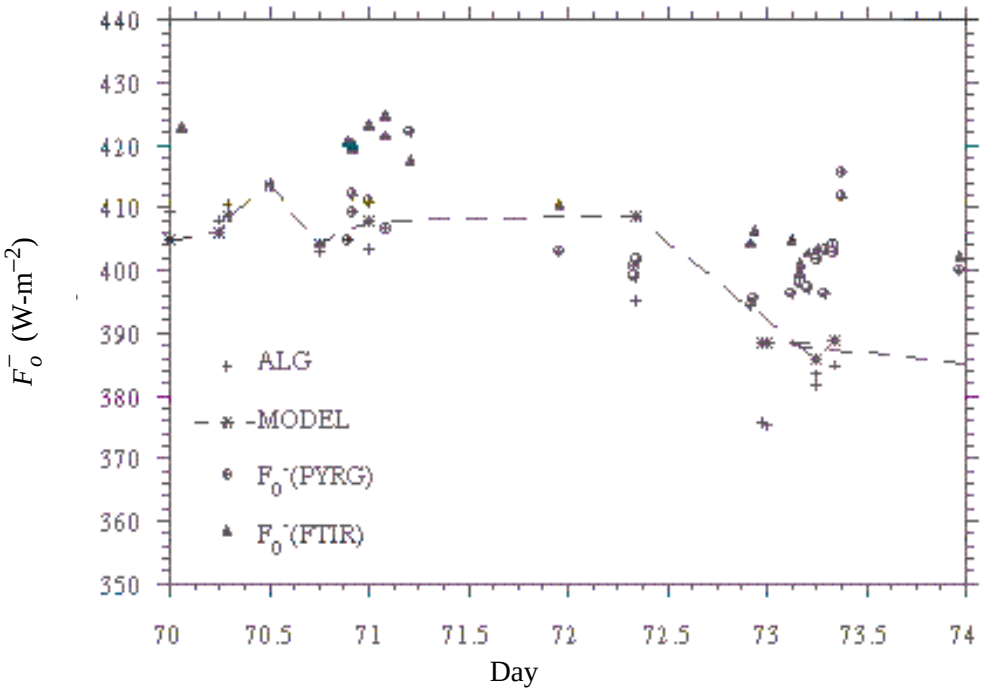

(a) Downward fluxes computed from radiative transfer model (continuous dashed line), predicted by algorithm, derived from FTIR-measured radiances, and also broadband flux measured by pyrgeometer aboard Vickers ship.

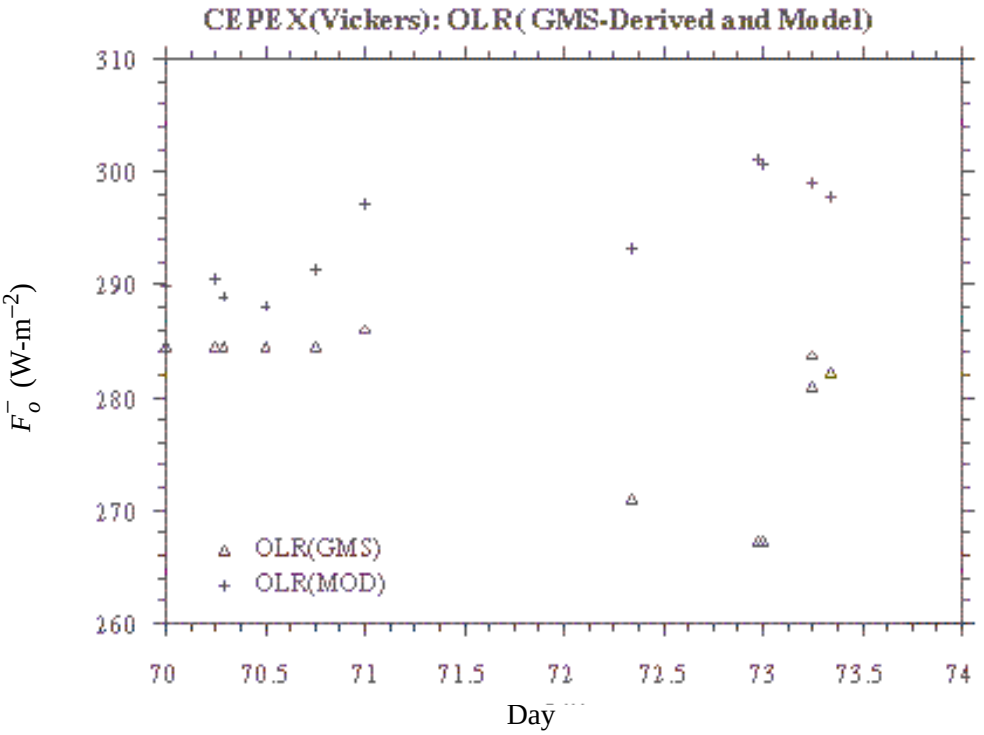

(b) Model-simulated outgoing longwave fluxes and those derived from GMS-observed infrared brightness temperature. The latter were used in algorithm estimates of flux.

Figure 12. Computed, predicted, and derived fluxes.

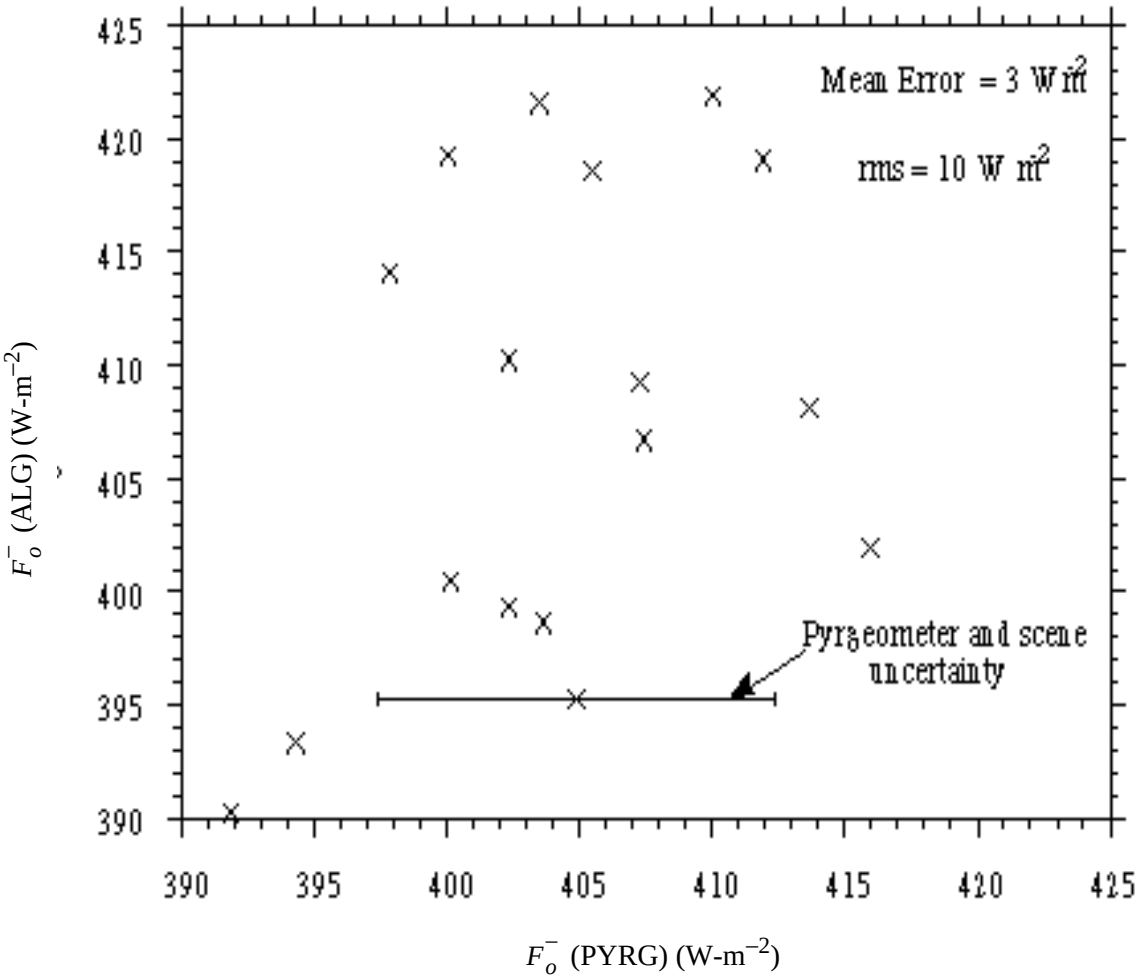

Figure 13. Time series of downward fluxes obtained from radiometer observations and algorithm at Kavieng Island (Nov. 1992 to Feb. 1993). TOA fluxes used in algorithm are from model.

Validation studies employing data from the CEPEX and ARM Probe sites indicate a reasonable agreement between the measurements and the parameterized flux estimates within the limits of uncertainties posed by the errors in scene identification, instrument calibration and/or aerosol emissions in the lower atmosphere, and modeling of the continuum absorption in the window. Sensitivity studies (not reported here) have revealed that thick haze in the atmospheric boundary layer (horizontal visibilities <15 km) could enhance the downward emissions by about 3–5 W-m^{-2}. Measurements at the ARM sites at Oklahoma and Kavieng also support this fact. Although there have been few, if any, simultaneous measurements of aerosols and longwave fluxes in the atmosphere to validate, a proposal to add an additional parameter in the form of aerosol visible optical depth in the future is under consideration.

4.6.2.5. References

Brutsaert, W. 1975: On a Derivable Formula for Longwave Radiation From Clear Skies. *Water Resour. Res.,* vol. 11, pp. 742–744.

Cess, R. D.; and Tiwari, S. N. 1972: Infrared Radiative Energy Transfer on Gasses. *Adv. Heat Transf*., vol. 8, pp. 229–283.

Clough, S. A.; and Brown, P. D. 1995: The Water Vapor Continuum and its Role in Remote Sensing. Abstract Volume of the 1995 OSA Tropical Meeting on the *Optical Remote Sensing of the Atmosphere.*

Clough, S. A.; Kneizys, F. X.; and Davies, R. W. 1989. Line Shape and the Water Vapor Continuum. *Atmos. Res.*, vol. 23, pp. 229–241.

Darnell, Wayne L.; Gupta, Shashi K.; and Staylor, W. Frank 1983: Downward Longwave Radiation at the Surface From Satellite Measurements. *J. Climat. & Appl. Meteorol.*, vol. 22, pp. 1956–1960.

Ellingson, Robert G.; Ellis, James; and Fels, Stephen 1991: The Intercomparison of Radiation Codes Used in Climate Models—Long Wave Results. *J. Geophys. Res.*, vol. 96, pp. 8929–8953.

Elliot, W. P.; and Gaffen, D. J. 1991: On the Utility of Radiosonde Humidity Archives for Climate Studies. *Bull. Am. Meteorol. Soc.*, vol. 72, pp. 1507–1520.

Frouin, Robert; Gautier, Catherine; and Morcrette, Jean-Jacques 1988: Downward Longwave Irradiance at the Ocean Surface From Satellite Data—Methodology and in Situ Validation. *J. Geophys. Res*., vol. 93, pp. 597–619.

Gupta, Shashi K. 1989: A Parameterization for Longwave Surface Radiation From Sun-Synchronous Satellite Data. *J. Climat.*, vol. 2, pp. 305–320.

Idso, S. B. 1981: On the Systematic Nature of Diurnal Patterns of Differences Between Calculations and Measurements of Clear Sky Atmospheric Thermal Radiation. *Q. J. R. Meteorol. Soc*., vol. 107, pp. 737–741.

Inamdar, A. K.; and Ramanathan, V. 1994: Physics of Greenhouse Effect and Convection in Warm Oceans. *J. Climat.*, vol. 7, no. 5, pp. 715–731.

Kneizys, F. X.; Shettle, E. P.; Abreu, L. W.; Chetwynd, J. H.; Anderson, G. P.; Gallery, W. O.; Selby, J. E. A.; and Clough, S. A. 1988: *Users Guide to LOWTRAN 7*. AFGL-TR-88-0177, U.S. Air Force.

Lubin, D. 1994: Infrared Radiative Properties of the Maritime Antarctic Atmosphere. *J. Climat.* vol. 7, pp. 121–140.

Raval, A.; and Ramanathan, V. 1989: Observational Determination of the Greenhouse Effect. *Nature*, vol. 342, pp. 758–761.

Schmetz, P.; Schmetz, J.; and Raschke, E. 1986: Estimation of Daytime Downward Longwave Radiation at the Surface From Satellite and Grid Point Data, *Theor. Appl. Climatol.*, vol. 37, pp. 136–149.

Tuzet, Andree 1990: A Simple Method for Estimating Downward Longwave Radiation From Surface and Satellite Data by Clear Sky. *Int. J. Remote Sens.*, vol. 11, pp. 125–131.

Wu, M. C.; and Cheng, C. P. 1989: Surface Downward Flux Computed by Using Geophysical Parameters Derived From HIRS 2/MSU Soundings. *Theor. Appl. Climatol.*, vol. 40, pp. 37–51.

Appendix

Nomenclature

Acronyms

ADEOS	Advanced Earth Observing System
ADM	Angular Distribution Model
AIRS	Atmospheric Infrared Sounder (EOS-AM)
AMSU	Advanced Microwave Sounding Unit (EOS-PM)
APD	Aerosol Profile Data
APID	Application Identifier
ARESE	ARM Enhanced Shortwave Experiment
ARM	Atmospheric Radiation Measurement
ASOS	Automated Surface Observing Sites
ASTER	Advanced Spaceborne Thermal Emission and Reflection Radiometer
ASTEX	Atlantic Stratocumulus Transition Experiment
ASTR	Atmospheric Structures
ATBD	Algorithm Theoretical Basis Document
AVG	Monthly Regional, Average Radiative Fluxes and Clouds (CERES Archival Data Product)
AVHRR	Advanced Very High Resolution Radiometer
BDS	Bidirectional Scan (CERES Archival Data Product)
BRIE	Best Regional Integral Estimate
BSRN	Baseline Surface Radiation Network
BTD	Brightness Temperature Difference(s)
CCD	Charge Coupled Device
CCSDS	Consultative Committee for Space Data Systems
CEPEX	Central Equatorial Pacific Experiment
CERES	Clouds and the Earth’s Radiant Energy System
CID	Cloud Imager Data
CLAVR	Clouds from AVHRR
CLS	Constrained Least Squares
COPRS	Cloud Optical Property Retrieval System
CPR	Cloud Profiling Radar
CRH	Clear Reflectance, Temperature History (CERES Archival Data Product)
CRS	Single Satellite CERES Footprint, Radiative Fluxes and Clouds (CERES Archival Data Product)
DAAC	Distributed Active Archive Center
DAC	Digital-Analog Converter
DAO	Data Assimilation Office

DB	Database
DFD	Data Flow Diagram
DLF	Downward Longwave Flux
DMSP	Defense Meteorological Satellite Program
EADM	ERBE-Like Albedo Directional Model (CERES Input Data Product)
ECA	Earth Central Angle
ECLIPS	Experimental Cloud Lidar Pilot Study
ECMWF	European Centre for Medium-Range Weather Forecasts
EDDB	ERBE-Like Daily Data Base (CERES Archival Data Product)
EID9	ERBE-Like Internal Data Product 9 (CERES Internal Data Product)
EOS	Earth Observing System
EOSDIS	Earth Observing System Data Information System
EOS-AM	EOS Morning Crossing Mission
EOS-PM	EOS Afternoon Crossing Mission
ENSO	El Niño/Southern Oscillation
ENVISAT	Environmental Satellite
EPHANC	Ephemeris and Ancillary (CERES Input Data Product)
ERB	Earth Radiation Budget
ERBE	Earth Radiation Budget Experiment
ERBS	Earth Radiation Budget Satellite
ESA	European Space Agency
ES4	ERBE-Like S4 Data Product (CERES Archival Data Product)
ES4G	ERBE-Like S4G Data Product (CERES Archival Data Product)
ES8	ERBE-Like S8 Data Product (CERES Archival Data Product)
ES9	ERBE-Like S9 Data Product (CERES Archival Data Product)
FLOP	Floating Point Operation
FIRE	First ISCCP Regional Experiment
FIRE II IFO	First ISCCP Regional Experiment II Intensive Field Observations
FOV	Field of View
FSW	Hourly Gridded Single Satellite Fluxes and Clouds (CERES Archival Data Product)
FTM	Functional Test Model
GAC	Global Area Coverage (AVHRR data mode)
GAP	Gridded Atmospheric Product (CERES Input Data Product)
GCIP	GEWEX Continental-Phase International Project
GCM	General Circulation Model
GEBA	Global Energy Balance Archive
GEO	ISSCP Radiances (CERES Input Data Product)
GEWEX	Global Energy and Water Cycle Experiment
GLAS	Geoscience Laser Altimetry System

GMS	Geostationary Meteorological Satellite
GOES	Geostationary Operational Environmental Satellite
HBTM	Hybrid Bispectral Threshold Method
HIRS	High-Resolution Infrared Radiation Sounder
HIS	High-Resolution Interferometer Sounder
ICM	Internal Calibration Module
ICRCCM	Intercomparison of Radiation Codes in Climate Models
ID	Identification
IEEE	Institute of Electrical and Electronics Engineers
IES	Instrument Earth Scans (CERES Internal Data Product)
IFO	Intensive Field Observation
INSAT	Indian Satellite
IOP	Intensive Observing Period
IR	Infrared
IRIS	Infrared Interferometer Spectrometer
ISCCP	International Satellite Cloud Climatology Project
ISS	Integrated Sounding System
IWP	Ice Water Path
LAC	Local Area Coverage (AVHRR data mode)
LaRC	Langley Research Center
LBC	Laser Beam Ceilometer
LBTM	Layer Bispectral Threshold Method
Lidar	Light Detection and Ranging
LITE	Lidar In-Space Technology Experiment
Lowtran 7	Low-Resolution Transmittance (Radiative Transfer Code)
LW	Longwave
LWP	Liquid Water Path
LWRE	Longwave Radiant Excitance
MAM	Mirror Attenuator Mosaic
MC	Mostly Cloudy
MCR	Microwave Cloud Radiometer
METEOSAT	Meteorological Operational Satellite (European)
METSAT	Meteorological Satellite
MFLOP	Million FLOP
MIMR	Multifrequency Imaging Microwave Radiometer
MISR	Multiangle Imaging Spectroradiometer
MLE	Maximum Likelihood Estimate
MOA	Meteorology Ozone and Aerosol
MODIS	Moderate-Resolution Imaging Spectroradiometer

MSMR	Multispectral, multiresolution
MTSA	Monthly Time and Space Averaging
MWH	Microwave Humidity
MWP	Microwave Water Path
NASA	National Aeronautics and Space Administration
NCAR	National Center for Atmospheric Research
NCEP	National Centers for Environmental Prediction
NESDIS	National Environmental Satellite, Data, and Information Service
NIR	Near Infrared
NMC	National Meteorological Center
NOAA	National Oceanic and Atmospheric Administration
NWP	Numerical Weather Prediction
OLR	Outgoing Longwave Radiation
OPD	Ozone Profile Data (CERES Input Data Product)
OV	Overcast
PC	Partly Cloudy
POLDER	Polarization of Directionality of Earth's Reflectances
PRT	Platinum Resistance Thermometer
PSF	Point Spread Function
PW	Precipitable Water
RAPS	Rotating Azimuth Plane Scan
RPM	Radiance Pairs Method
RTM	Radiometer Test Model
SAB	Sorting by Angular Bins
SAGE	Stratospheric Aerosol and Gas Experiment
SARB	Surface and Atmospheric Radiation Budget Working Group
SDCD	Solar Distance Correction and Declination
SFC	Hourly Gridded Single Satellite TOA and Surface Fluxes (CERES Archival Data Product)
SHEBA	Surface Heat Budget in the Arctic
SPECTRE	Spectral Radiance Experiment
SRB	Surface Radiation Budget
SRBAVG	Surface Radiation Budget Average (CERES Archival Data Product)
SSF	Single Satellite CERES Footprint TOA and Surface Fluxes, Clouds
SSMI	Special Sensor Microwave Imager
SST	Sea Surface Temperature
SURFMAP	Surface Properties and Maps (CERES Input Product)
SW	Shortwave
SWICS	Shortwave Internal Calibration Source

SWRE	Shortwave Radiant Excitance
SYN	Synoptic Radiative Fluxes and Clouds (CERES Archival Data Product)
SZA	Solar Zenith Angle
THIR	Temperature/Humidity Infrared Radiometer (Nimbus)
TIROS	Television Infrared Observation Satellite
TISA	Time Interpolation and Spatial Averaging Working Group
TMI	TRMM Microwave Imager
TOA	Top of the Atmosphere
TOGA	Tropical Ocean Global Atmosphere
TOMS	Total Ozone Mapping Spectrometer
TOVS	TIROS Operational Vertical Sounder
TRMM	Tropical Rainfall Measuring Mission
TSA	Time-Space Averaging
UAV	Unmanned Aerospace Vehicle
UT	Universal Time
UTC	Universal Time Code
VAS	VISSR Atmospheric Sounder (GOES)
VIRS	Visible Infrared Scanner
VISSR	Visible and Infrared Spin Scan Radiometer
WCRP	World Climate Research Program
WG	Working Group
Win	Window
WN	Window
WMO	World Meteorological Organization
ZAVG	Monthly Zonal and Global Average Radiative Fluxes and Clouds (CERES Archival Data Product)

Symbols

A	atmospheric absorptance
$B_\lambda(T)$	Planck function
C	cloud fractional area coverage
CF_2Cl_2	dichlorofluorocarbon
$CFCl_3$	trichlorofluorocarbon
CH_4	methane
CO_2	carbon dioxide
D	total number of days in the month
D_e	cloud particle equivalent diameter (for ice clouds)
E_o	solar constant or solar irradiance
F	flux

f	fraction
G_a	atmospheric greenhouse effect
g	cloud asymmetry parameter
H_2O	water vapor
I	radiance
i	scene type
m_i	imaginary refractive index
$\hat{N}$	angular momentum vector
N_2O	nitrous oxide
O_3	ozone
P	point spread function
p	pressure
Q_a	absorption efficiency
Q_e	extinction efficiency
Q_s	scattering efficiency
R	anisotropic reflectance factor
r_E	radius of the Earth
r_e	effective cloud droplet radius (for water clouds)
r_h	column-averaged relative humidity
S_o	summed solar incident SW flux
S_o'	integrated solar incident SW flux
T	temperature
T_B	blackbody temperature
t	time or transmittance
W_{liq}	liquid water path
w	precipitable water
$\hat{x}_o$	satellite position at t_o
x, y, z	satellite position vector components
$\dot{x}, \dot{y}, \dot{z}$	satellite velocity vector components
z	altitude
z_{top}	altitude at top of atmosphere
α	albedo or cone angle
β	cross-scan angle
γ	Earth central angle
γ_{at}	along-track angle
γ_{ct}	cross-track angle
δ	along-scan angle
ε	emittance
Θ	colatitude of satellite

θ	viewing zenith angle
θ_o	solar zenith angle
λ	wavelength
μ	viewing zenith angle cosine
μ_o	solar zenith angle cosine
ν	wave number
ρ	bidirectional reflectance
τ	optical depth
$\tau_{aer}(p)$	spectral optical depth profiles of aerosols
$\tau_{H_2O\lambda}(p)$	spectral optical depth profiles of water vapor
$\tau_{O_3}(p)$	spectral optical depth profiles of ozone
Φ	longitude of satellite
ϕ	azimuth angle
$\tilde{\omega}_o$	single-scattering albedo

Subscripts:

c	cloud
cb	cloud base
ce	cloud effective
cld	cloud
cs	clear sky
ct	cloud top
ice	ice water
lc	lower cloud
liq	liquid water
s	surface
uc	upper cloud
λ	spectral wavelength

Units

AU	astronomical unit
cm	centimeter
cm-sec^{-1}	centimeter per second
count	count
day	day, Julian date
deg	degree
deg-sec^{-1}	degree per second
DU	Dobson unit
erg-sec^{-1}	erg per second
fraction	fraction (range of 0–1)

g	gram
g-cm^{-2}	gram per square centimeter
g-g^{-1}	gram per gram
g-m^{-2}	gram per square meter
h	hour
hPa	hectopascal
K	Kelvin
kg	kilogram
kg-m^{-2}	kilogram per square meter
km	kilometer
km-sec^{-1}	kilometer per second
m	meter
mm	millimeter
μm	micrometer, micron
N/A	not applicable, none, unitless, dimensionless
ohm-cm^{-1}	ohm per centimeter
percent	percent (range of 0–100)
rad	radian
rad-sec^{-1}	radian per second
sec	second
sr^{-1}	per steradian
W	watt
W-m^{-2}	watt per square meter
W-m^{-2}sr^{-1}	watt per square meter per steradian
W-m^{-2}sr^{-1}μm^{-1}	watt per square meter per steradian per micrometer